clearity clusters most probably involves interchain interactions. A plausible transformation is illustrated in Figure 9. Here, a M_3E_4 unit (half of M_6E_8) is built up from two metals in one chain and one metal in a neighboring chain. The chalcogenide that bridged the two chains in ME_3 becomes the "cap" of the M_3E_4 unit. The other half of the M_6E_8 cluster can be imagined to be contributed by another layer of interacting ME_3 chains. Of course, the EXAFS alone can shed no light on the nature of the intermediate structures involved in such a transformation. Perhaps other experiments could better address this point.

Summary

EXAFS analysis has shown that lithiation of the amorphous materials MoS_3, WS_3, and WSe_3 results in a condensation into larger metal cluster, which may be similar to the clusters found in Chevrel-phase structures. This result is consistent with chemical trends previously observed in molecular cluster chemistry. These lithiated materials represent a unique transition region between small molecular clusters and the solid state, and they may be of synthetic value in the creation of large metal-chalcogenide clusters.

Acknowledgment. The X-ray absorption measurements were performed at the Stanford Synchrotron Radiation Laboratory (SSRL), which is supported by the Department of Energy, Office of Basic Energy Sciences. The work was performed while R.A.S. was at Stanford as a NIH Postdoctoral Fellow. XAS work under K.O.H. is supported by the NSF and NIH.

Registry No. MoS_3, 12033-29-3; WS_3, 12125-19-8; WSe_3, 88981-34-4; $NbSe_3$, 12034-78-5; Li_4MoS_3, 76770-55-3; Li_4WS_3, 101011-07-8; Li_5WSe_3, 101011-08-9; Li_3NbSe_3, 55886-04-9; MoS_2, 1317-33-5; $[Mo_2(S_2)_6]^{2-}$, 97278-58-5; $[Mo_3(S)(S_2)_6]^{2-}$, 88765-92-8; WS_2, 12138-09-9; WSe_2, 12067-46-8; $[WSe_4]^{2-}$, 21559-01-3; $NbSe_2$, 12034-77-4; Se, 7782-49-2; $[Fe_2Se_2(CO)_6]^{2-}$, 101011-09-0; $Fe_2Se_2(CO)_6$, 76185-26-7; Li, 7439-93-2; $LiMoS_3$, 101011-10-3; Li_2MoS_3, 101011-11-4; Li_3MoS_3, 101011-12-5.

Supplementary Material Available: Table II, containing reanalysis of curve fitting for the structurally characterized compounds MoS_2, $[Mo_2(S_2)_6]^{2-}$, $[Mo_3(S)(S_2)_6]^{2-}$, WS_2, WSe_2, $[WSe_4]^{2-}$, $NbSe_2$, and Se^0 (3 pages). Ordering information is given on any current masthead page.

Contribution from the School of Chemical Sciences, University of Illinois, Urbana, Illinois 61801

Structural Evidence Concerning the Frontier Orbitals in $[Fe_2E_2(CO)_6]^{2-}$ (E = S, Se): Redox-Active Dichalcogen Ligands

Timothy D. Weatherill, Thomas B. Rauchfuss,* and Robert A. Scott*

Received October 18, 1985

Fe and Se extended X-ray absorption fine structure (EXAFS) data have been used to determine the structures of the Fe_2E_2 (E = S, Se) cores of the following compounds: $[Fe_2E_2(CO)_6]^z$ (z = 0, 2-), $Fe_2(\mu\text{-}ER)_2(CO)_6$ (R = alkyl), $[Fe_2E_2(NO)_4]^{2-}$, and $Fe_2(\mu\text{-}ER)_2(NO)_4$. For the carbonyl compounds, the Fe EXAFS results indicate that the Fe–C, Fe–Fe, and Fe–E distances change little upon conversion of $Fe_2(E_2)(CO)_6$ to $[Fe_2E_2(CO)_6]^{2-}$ and $Fe_2(\mu\text{-}ER)_2(CO)_6$. The Se EXAFS results are consistent with the Fe EXAFS data, also showing that the two-electron reduction of $Fe_2(Se_2)(CO)_6$ results in breaking of the Se–Se bond. The Fe and Se EXAFS of the related nitrosyls $[Fe_2E_2(NO)_4]^{2-}$ and $Fe_2(\mu\text{-}ER)_2(NO)_4$ confirm that the Fe_2E_2 cores of these complexes are similar. All of the EXAFS results are consistent with the LUMO of $Fe_2(E_2)(CO)_6$, being mainly E–E antibonding in character.

Introduction

Since its preparation in the mid-1950s,[1] the compound $Fe_2(S_2)(CO)_6$ has been the subject of a number of investigations. Its solid-state structure as determined by Wei and Dahl features a tetrahedral Fe_2S_2 core, acute Fe–S–Fe angles, and a short Fe–Fe distance of 2.55 Å.[2] On the basis of this data, all atoms within the Fe_2S_2 core are considered to be mutually bonded. Several theoretical studies have dealt with the bonding and electronic structure of this species, the nature of the Fe–Fe bond being the primary focus.[3,4] Wei and Dahl suggested that the structure of $Fe_2(S_2)(CO)_6$ is due in part to the presence of a "bent" Fe–Fe bond. The origin of the iron orbitals responsible for this bond may be found by considering each iron atom as being octahedrally coordinated, the Fe–Fe bond arising from orbitals occupying the (sixth) position trans to the axial carbonyl ligands. Teo et al. supported this interpretation with a Fenske–Hall calculation and assigned the HOMO and LUMO to the bonding and antibonding components of the Fe–Fe interaction.[4] An ab initio calculation also describes the Fe–Fe interaction in terms of a "bent" bond and assigns this molecular orbital as the HOMO.[5] Self-consistent-field Xα scattered-wave molecular orbital calculations done by Andersen et al., provide a modified picture of the bonding situation in $Fe_2(S_2)(CO)_6$.[6] The SCF-Xα-SW results, together with a He I photoelectron study, indicate that the S_2 bridge enhances and stabilizes the π-component of the Fe–Fe bond. The assertion by Andersen et al. that the Fe–Fe bond possesses some multiple-bond character has been disputed by DeKock and co-workers on the basis of He I and He II photoelectron spectroscopy and Hartree–Fock–Slater calculations.[7] They argue that the LUMO in $Fe_2(S_2)(CO)_6$ is antibonding with respect to the sulfur atoms, not the iron atoms.

The chemistry of the dianion $[Fe_2S_2(CO)_6]^{2-}$ suggests that the LUMO in $Fe_2(S_2)(CO)_6$ is indeed primarily S–S antibonding.[8] Thus, Seyferth and co-workers have demonstrated that the reactivity of $[Fe_2S_2(CO)_6]^{2-}$ is sulfur-localized. Alkylation and metalation of this dianion afford neutral $Fe_2(\mu\text{-}SR)_2(CO)_6$ derivatives: the integrity of the Fe–Fe bond is retained in the products (eq 1).

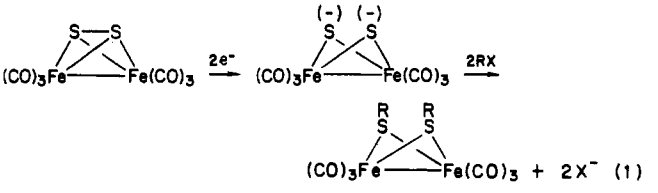

(1)

Although the structures of these alkylated and metalated products are firmly established, the structure of the parent dianion remains unknown. Herein we report the determination of the

(1) Hieber, W.; Gruber, J. *Z. Anorg. Allg. Chem.* **1958**, *296*, 91.
(2) Wei, C. H.; Dahl, L. F. *Inorg. Chem.* **1965**, *4*, 493. Wei, C. H.; Dahl, L. F. *Inorg. Chem.* **1965**, *4*, 1.
(3) For related theoretical discussions see: Burdett, J. K. *J. Chem. Soc., Dalton Trans.* **1977**, 423. Summerville, R. H.; Hoffmann, R. *J. Am. Chem. Soc.* **1976**, *98*, 7240. Mason, R.; Mingos, D. M. P. *J. Organomet. Chem.* **1973**, *50*, 53. Teo, B. K.; Hall, M. B.; Fenske, R. G.; Dahl, L. F. *J. Organomet. Chem.* **1974**, *70*, 413.
(4) Teo, B. K.; Hall, M. B.; Fenske, R. F.; Dahl, L. F. *Inorg. Chem.* **1975**, *14*, 3103.
(5) Van Dam, H.; Louwen, J. N.; Oskam, A.; Doran, M.; Hillier, I. H. *J. Electron Spectrosc. Relat. Phenom.* **1980**, *21*, 57.
(6) Andersen, E. L.; Fehlner, T. P.; Foti, A. E.; Salahub, D. R. *J. Am. Chem. Soc.* **1980**, *102*, 7422.
(7) DeKock, R. L.; Baerends, E. J; Hengelmolen, R. *Organometallics* **1984**, *3*, 289. DeKock, R. L.; Baerends, E. J.; Hengelmolen, R. *Inorg. Chem.* **1983**, *22*, 4158.
(8) Seyferth, D.; Henderson, R. S. *Organometallics* **1982**, *1*, 125.

0020-1669/86/1325-1466$01.50/0

solution structures of $[Fe_2S_2(CO)_6]^{2-}$, $[Fe_2Se_2(CO)_6]^{2-}$, and several related derivatives by Fe and Se EXAFS. Our results clearly demonstrate that reduction of $Fe_2E_2(CO)_6$ primarily affects the dichalcogen bond, leaving the Fe–Fe bond essentially intact. These results confirm that the LUMO in these tetrahedranes is not significantly antibonding with respect to the metal–metal interaction.

Experimental Section

Starting Materials and Reagents. The following compounds were prepared according to the indicated literature methods: $Fe_2S_2(CO)_6$,[9] $Fe_2(\mu\text{-SMe})_2(CO)_6$,[10] $Fe_2Se_2(CO)_6$,[11] $Fe_2(\mu\text{-SePh})_2(CO)_6$,[12] $Fe_2(\mu\text{-SEt})_2(NO)_4$,[13] and $Fe_2(\mu\text{-I})_2(NO)_4$.[14] The purity of these compounds was established by elemental analysis, thin-layer chromatography on silica gel, and infrared spectroscopy (ν_{CO} or ν_{NO} region).

The following materials were obtained from the standard commercial sources and were used without further purification: $LiBEt_3H$ (1.0 M in THF), PhSeSePh, $(1,3\text{-}C_4H_6)Fe(CO)_3$, $AsPh_4Cl\cdot H_2O$, $Na_2S\cdot 9H_2O$, gray Se, and boron nitride (BN). Benzyl chloride and methyl iodide were stored over 4A molecular sieves prior to use. Reagent grade methanol was thoroughly sparged with nitrogen prior to use.

Carbonyl Anions. Preparation of THF solutions of $Li_2[Fe_2E_2(CO)_6]$ (E = S, Se) was performed in a nitrogen-filled inert-atmosphere (O_2 < 1.0 ppm) chamber (Vacuum Atmospheres) in the Biotechnology Laboratory at the Stanford Synchrotron Radiation Laboratory (SSRL). THF was freshly distilled from sodium benzophenone ketyl. A 0.07 M solution of $Fe_2(S_2)(CO)_6$ was prepared by dissolving 96 mg of the solid in 4.0 mL of THF in a septum-capped flask. The $Li_2[Fe_2S_2(CO)_6]$ solution was generated by slow addition of 0.58 mL of $LiBEt_3H$ to the red solution of $Fe_2(S_2)(CO)_6$ at ambient temperature. A 250-μL aliquot of the now green solution was withdrawn by using a gastight syringe and loaded into an anaerobic solution EXAFS cell consisting of a Nylon body and Mylar windows and having a 1-mm X-ray path length. The cell was sealed with rubber septa and mounted in a Mylar shroud that was continuously purged with dry He during data collection. The integrity of the green $[Fe_2S_2(CO)_6]^{2-}$ solution was checked visually and also experimentally by treating the solution with MeI, which gave the characteristic orange color of $Fe_2(\mu\text{-SMe})_2(CO)_6$. EXAFS spectra of the $Fe_2(S_2)(CO)_6$ and $Fe_2(\mu\text{-SMe})_2(CO)_6$ solutions were recorded and found to be identical with the spectra of authentic solid samples of these compounds. $Li_2[Fe_2Se_2(CO)_6]$ solutions were generated in a completely analogous manner and EXAFS spectra of $Li_2[Fe_2E_2(CO)_6]$ (E = S, Se) solutions were recorded within 1 h of preparation.

Since a slight excess of $LiBEt_3H$ (2.1 equiv) is used to generate solutions of $Li_2[Fe_2E_2(CO)_6]$ (E = S, Se), it was necessary to ascertain whether the dianions further react with $LiBEt_3H$. The following experiment also demonstrates that solutions of $Li_2[Fe_2E_2(CO)_6]$ (E = S, Se) maintain their integrity over the period of time they were under study by EXAFS. A 0.05 M solution of $Fe_2(S_2)(CO)_6$ (172 mg in 10 mL of THF) was treated consecutively with 1.0, 2.0, 2.5, and 3.0 equiv of $LiBEt_3H$. Monitoring the reaction by FTIR spectroscopy showed that the neutral dimer was completely absent after the addition of 1.0 equiv. The IR spectrum of this monoreduced species differed significantly from the spectrum of the green $Li_2[Fe_2S_2(CO)_6]$ solution produced after addition of 2.0 equiv. This spectrum did not change over a period of 3 h and also did not change when an excess of $LiBEt_3H$ was added. Treatment of the green reaction mixture with a slight excess of MeI (0.093 mL, 1.5 mmol) produced an orange solution, which was evaporated to give an orange solid. Upon purification, this solid was identified as a 90% yield of pure $Fe_2(\mu\text{-SMe})_2(CO)_6$.

Nitrosyl Anions. Beck and co-workers have reported the metathetical synthesis of $(AsPh_4)_2[Fe_2S_2(NO)_4]$ from Roussin's red sodium salt $Na_2[Fe_2S_2(NO)_4]$;[15] below we present syntheses of $(AsPh_4)_2[Fe_2E_2(NO)_4]$ (E = S, Se) directly from the readily available $Fe_2(\mu\text{-I})_2(NO)_4$.

A 520-mg (2.1-mmol) sample of $Na_2S\cdot 9H_2O$ and 5 g of NaOH were dissolved in 200 mL of MeOH and 50 mL of H_2O. The solution was warmed to 50 °C and treated with 500 mg (1.03 mmol) of $Fe_2(\mu\text{-I})_2(NO)_4$. The deep red solution was filtered through a medium frit and treated with 1.2 g (2.5 mmol) of $AsPh_4Cl\cdot H_2O$. The volume of the solution was reduced by about half to give lustrous red crystals of $(AsPh_4)_2[Fe_2S_2(NO)_4]$, which were collected and extensively washed with H_2O. The yield was 900 mg (88%). Anal. Calcd for $C_{48}H_{40}N_4Fe_2S_2As_2O_4$: C, 54.26; H, 3.79; N, 5.27; Fe, 10.51. Found: C, 53.72; H, 3.75; N, 5.45; Fe, 10.73. The infrared spectrum of a KBr pellet showed ν_{NO} bands at 1617 and 1658 cm^{-1}.

For $(AsPh_4)_2[Fe_2Se_2(NO)_4]$, 237 mg (3.0 mmol) of Se powder and 10 g of NaOH were added to 100 mL of EtOH and 50 mL of H_2O. A 284-mg (7.5-mmol) sample of $NaBH_4$ was added to the slurry and the mixture heated to 75 °C for 3 h. Treatment of the red solution with 728 mg (1.5 mmol) of $Fe_2(\mu\text{-I})_2(NO)_4$ produced a dark red solution, which was filtered and reheated to 50 °C. Addition of 1.5 g (3.43 mmol) of $AsPh_4Cl\cdot H_2O$ in 10 mL of H_2O, followed by vigorous stirring, produced dark red crystals. After cooling to room temperature, the solution was filtered, and the crystals were extensively washed with H_2O. Drying the crystals in vacuo gave a yield of 1.20 g (70%). Anal. Calcd for $C_{48}H_{40}N_4Fe_2Se_2As_2O_4$: C, 49.85; H, 3.48; N, 4.85. Found: C, 49.37; H, 3.35; N, 4.75. The infrared spectrum of a KBr pellet showed ν_{NO} bands at 1628 and 1660 cm^{-1}.

Solid-Sample Preparation. Solid samples were prepared for EXAFS measurements by grinding to a fine powder and diluting with BN, followed by further grinding of the mixture. The samples were prepared aerobically, as none of the solids are particularly sensitive to oxygen. The ground samples were loaded into slots cut in 0.76-mm-thick aluminum plates and sealed with Mylar tape.

Data Collection and Reduction. Fe K-edge XAS data were collected at SSRL on either beam line VII-3 or beam line II-2 (focused). Most of the data were collected under parasitic conditions at 1.88 GeV (ca. 15 mA beam current), with the remainder acquired under dedicated conditions at 3.0 GeV (ca. 50 mA). Se K-edge XAS transmission data were collected on beam line VII-3 (SSRL) under parasitic conditions as described above. In all cases, the synchrotron radiation was monochromatized by using Si[220] crystals. The data were collected at high resolution (1-mm vertical aperture), and the samples were at ambient temperature.

The raw XAS data were reduced to EXAFS data by standard techniques as follows. The energy scale was defined by the internal calibration technique[16] using an Fe foil or a spectroscopically thin sample of powdered elemental Se as reference (first inflection point of edge at 7111.2 and 12656.0 eV for Fe and Se K edges, respectively). Replicate spectra were then averaged together (two to seven spectra for each sample). The background absorbance was simulated by fitting a second-order polynomial to the raw data [i.e., $\ln (I_0/I)$] in a selected region before the edge of interest and subtracting the extrapolated polynomial from the entire data set. The fitting region for Fe EXAFS was 6680–7070 eV and for Se EXAFS, 12340–12620 eV. The smooth background in the EXAFS region of the resultant data was simulated by a cubic spline which for Fe EXAFS covered the region 7150–8170 eV with nodes at 7330 and 7650 eV and for Se EXAFS covered the region 12699–13491 eV with nodes at 12836 and 13093 eV. Subtraction of this cubic spline followed by normalization using the atomic falloff simulated by the Victoreen equation[17] resulted in the EXAFS data ($\chi(\mathbf{k})$) as a function of the photoelectron wave vector, $\mathbf{k}$. The $\mathbf{k}$ scale was defined to start ($\mathbf{k} = 0$) at 7130 eV (Fe) or 12675 eV (Se).

Typically, the data were collected to $\mathbf{k} = 14.5$ Å^{-1} and the $\chi(\mathbf{k})$ data were Fourier-transformed (over the range $\mathbf{k} = 3.5$–14.5 Å^{-1}; $\mathbf{k}^3$ weighting) in order to visualize the shells present. In all cases, curve fitting was performed on raw $\chi(\mathbf{k})$ data.

Data Analysis. The following EXAFS expression was used for curve fitting of the EXAFS data:

$$\chi(\mathbf{k}) = \sum_{i=1}^{n} \frac{N_i S_i |f_i(\pi,\mathbf{k})|}{\mathbf{k} R_i^2} [\exp(-2\sigma_i^2\mathbf{k}^2)] \sin [2\mathbf{k}R_i + \alpha_i(\mathbf{k})] \quad (2)$$

In this expression, the sum is over the n shells of scatterers (the shells being indexed by the i subscripts). N_i is the number of scatterers in the ith shell, R_i is the (average) distance between the absorber (Fe or Se) and the scatterers that make up the ith shell, σ_i^2 is the mean-square deviation in R_i, S_i is a scale factor (used to adjust theoretical amplitude functions), $|f_i(\pi,\mathbf{k})|$ is the inherent backscattering amplitude (as a function of $\mathbf{k}$) for scatterers of the ith shell, and $\alpha_i(\mathbf{k})$ is the inherent phase shift (as a function of $\mathbf{k}$) for scatterers of the ith shell. These amplitude

(9) Bogan, Jr., L. E.; Lesch, D. A.; Rauchfuss, T. B. *J. Organomet. Chem.* **1983**, *250*, 429.
(10) *Organometallic Syntheses*; Eisch, J. J., King, R. B., Eds.; Academic: New York, 1965; p 180.
(11) Seyferth, D.; Henderson, R. S. *J. Organomet. Chem.* **1981**, *204*, 333.
(12) Hieber, W.; Beck, W. *Z. Anorg. Allg. Chem.* **1965**, *305*, 265. Rosenbuch, P.; Welcman, N. *J. Chem. Soc., Dalton Trans.* **1972**, 1963.
(13) Rauchfuss, T.; Weatherill, T. D. *Inorg. Chem.* **1982**, *21*, 827.
(14) Haymore, B.; Feltham, R. D. *Inorg. Synth.* **1968**, *10*, 81.
(15) Beck, W.; Grenz, R.; Gotzfried, F.; Vilsmaier, E. *Chem. Ber.* **1981**, *114*, 3184.
(16) Scott, R. A. In *The Biological Chemistry of Iron*; Dunford, H. B., Dolphin, D. H., Raymond, K. N., Sieker, L. C., Eds.; Reidel: Boston, 1982; p 475.
(17) MacGillavry, C. H.; Rieck, G. D. *International Tables for X-Ray Crystallography*; Kynoch: Birmingham, England, 1968; Vol. 3, p 171.

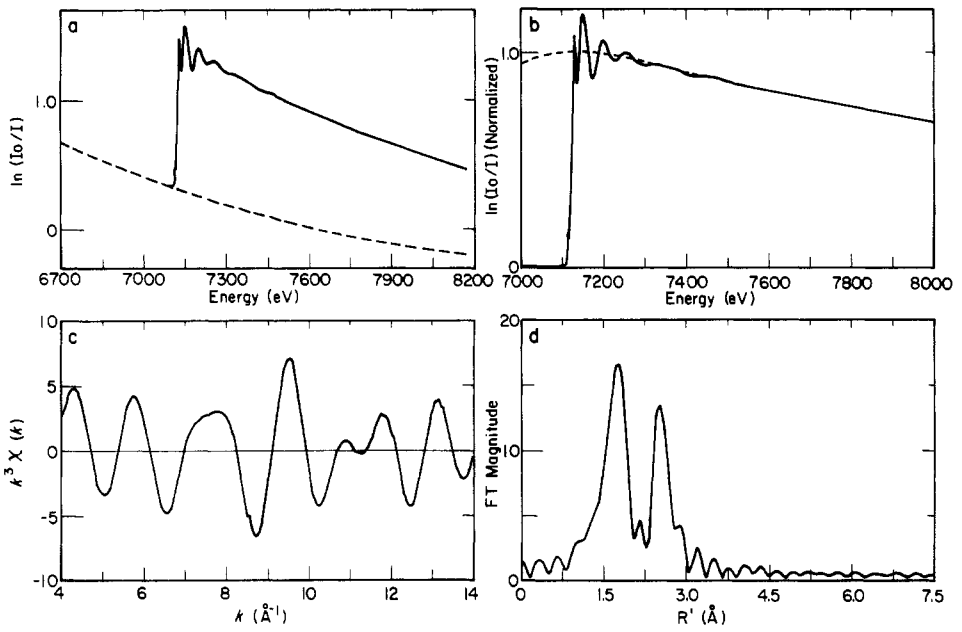

Figure 1. Example of XAS data reduction using Fe K-edge data from a solid sample of $Fe_2(S_2)(CO)_6$. (a) Correction for the background absorption is done by fitting a second-order polynomial (---) to the preedge region (6680–7070 eV) of the raw data (—) and subtracting. (b) After normalization of the result of (a), a third order spline (---) is fit to the data (—) in the EXAFS region (7150–8170 eV, with spline points at 7330, 7650 eV). Subtraction of this spline yields the EXAFS data. (c) The extracted EXAFS data are usually treated as a function of the photoelectron wave vector (**k**) and are shown here weighted by $\mathbf{k}^3$. (d) Fourier transformation ($\mathbf{k}$ = 3.5–14.5 Å^{-1}) of the $\mathbf{k}^3\chi(\mathbf{k})$ data in (c) yields a set of peaks in phase-shifted distance space (R'), each of which arises from a shell of scattering atoms.

and phase functions are specific for the atomic number of the atoms making up the ith shell, and much of the effort involved in EXAFS curve fitting is in generating these functions for each type of scatterer expected to contribute to the EXAFS.

Whenever possible, the amplitude and phase functions for a particular absorber–scatterer combination were extracted from EXAFS data on a structurally characterized "model" compound by complex Fourier back-transformation of an *isolated* Fourier transform (FT) peak. In some cases, structurally characterized examples of the $Fe_2(E_2)L_n$ or $Fe_2(\mu\text{-}ER)_2L_n$ series [L_n = $(CO)_6$, $(NO)_4$] were used as model compounds. For Fe EXAFS, amplitude and phase functions for the following absorber–scatterer combinations were required: Fe–C, Fe–N, Fe–S, Fe–Se, Fe–Fe, Fe–(C–)O, Fe–(N–)O. For Fe–N scattering, $Fe_2(\mu\text{-}SEt)_2(NO)_4$ was used as a model compound since the Fe–N FT peak was easily extracted (by Fourier filtering) from the other FT peaks. The crystallographic Fe–N distance of 1.67 Å[18] and N_i = 2 were used to extract the Fe–N amplitude and phase functions from this filter. The structurally characterized carbonyl dimers $(Fe_2(S_2)(CO)_6$ and $Fe_2(\mu\text{-}SMe)_2(CO)_6)$ yielded Fe EXAFS FTs with Fe–C peaks poorly separated from the other FT peaks. Thus, the amplitude and phase functions for Fe–N scattering were also used for Fe–C scattering. Curve fitting of Fe EXAFS of $Fe_2(S_2)(CO)_6$ and $Fe_2(\mu\text{-}SMe)_2(CO)_6$ indicated that more accurate fits of Fe–C were obtained by setting ΔE_0 to −5 eV in the Fe–N functions.

The FT peak assignable to Fe–(C–)O scattering in the carbonyl dimers appears to have an intensity approximately equal to those of the Fe–S or Fe–Se peaks due to a focusing effect in this collinear arrangement of atoms.[19] $Fe(1,3\text{-}C_4H_6)(CO)_3$ was used as a model compound for this interaction (in the carbonyl dimers, the Fe–(C–)O FT peak was not completely isolated from the Fe–Fe FT peak). For the analogous Fe–(N–)O scattering, no appropriate iron nitrosyl complexes were available for examination. Thus, the Fe–(C–)O amplitude and phase functions were used. The nonlinearity of the Fe–N–O moiety (e.g., the Fe–N–O angle is 167° in $Fe_2(\mu\text{-}SEt)_2(NO)_4$) results in a significantly smaller focusing effect than for Fe–(C–)O, yielding a lower scattering intensity. This difference was most conveniently handled by allowing σ_i^2 to vary, and significantly larger σ_i^2 values were found for Fe–(N–)O scattering compared to Fe–(C–)O scattering.

For Fe–S and Fe–Fe scattering, appropriate model compounds had been examined but the usable $\chi(\mathbf{k})$ data for each did not extend to $\mathbf{k}$ = 14 Å^{-1} (the end of the curve-fitting range used). In these cases, a procedure analogous to the FABM (fine adjustment based on models) approach[20] was used. Theoretical amplitude and phase functions were used to first fit the model compounds ($(NEt_4)[Fe(SR)_4]$, R = $C_{10}H_{13}$ (2,3,5,6-tetramethylbenzene),[21] was used for Fe–S, and $(NEt_4)_2[Fe_2S_2(S_2\text{-}o\text{-}xyl)_2]$[22] was used for Fe–Fe) over a reduced $\mathbf{k}$ range. Theoretical amplitude functions are generally found to be about twice too large and theoretical phase functions are often found to be on a different $\mathbf{k}$ scale than the one defined for the data by the (rather arbitrary) choice of E_0. Thus, in these initial fits, R_i and N_i were fixed (at the crystallographically determined values) and S_i, σ_i^2, and ΔE_0 were optimized. The values determined by these initial fits to the model compounds were S_i = 0.4, ΔE_0 = +1 eV (for Fe–S) and S_i = 0.4, ΔE_0 = −1 eV (for Fe–Fe). These values were used along with the theoretical amplitude and phase functions for all the fits discussed herein. This procedure may be thought of as using the theoretical forms of the amplitude and phase functions to extrapolate the empirical model compound data to larger $\mathbf{k}$ ranges.

For Fe–Se scattering, the only structurally characterized compound for which Fe EXAFS was available is $Fe_2(Se_2)(CO)_6$. The Fe–Se FT peak for this compound was not isolable from the other interactions, but since amplitude and phase functions were available for the other scatterers, a four-shell fit of the data using the known distances for the other shells and the theoretical Fe–Se amplitude and phase functions yielded S_i = 0.4, ΔE_0 = +2 eV as reasonable values for Fe–Se fits using theoretical functions.

For curve fitting of the Se EXAFS, Se–C, Se–Se, and Se–Fe scattering functions were required. The model compound diphenyl diselenide (PhSeSePh) was used to extract empirical Se–Se and Se–C amplitude and phase functions (with R_i = 2.29 Å, N_i = 1 for Se–Se and R_i = 1.93 Å, N_i = 1 for Se–C[23]) from easily separable Se–Se and Se–C peaks in the FT of the Se EXAFS of this compound. For Se–Fe scattering, the only structurally characterized compound examined was $Fe_2(Se_2)(CO)_6$. The Se EXAFS of this compound exhibits a single FT peak consisting of both Se–Se and Se–Fe scattering. As discussed below, this FT peak is nearly twice the size of the Se–Se FT peak of PhSeSePh. The extra FT intensity must be due to the Se–Fe scattering, and a two-shell (Se–Se, Se–Fe) fit using theoretical Se–Fe amplitude and phase functions yielded S_i = 0.6, ΔE_0 = +9 eV as the values to use for theoretical function-based fitting of Se–Fe interactions.

The final curve-fitting procedures for the compounds of unknown structure consisted of multiple-shell simulations of the raw data over the

(18) Thomas, J. T.; Robertson, J. H.; Cox,, E. G. *Acta Crystallogr.* **1958**, *11*, 599.
(19) Teo, B.-K. *J. Am. Chem. Soc.* **1981**, *103*, 3990.
(20) Teo, B.-K.; Antonio, M. R.; Averill, B. A. *J. Am. Chem. Soc.* **1983**, *105*, 3751.
(21) This sample was a gift from S. A. Koch. See: Millar, M.; Lee, J. F.; Koch, S. A.; Fikar, R. *Inorg. Chem.* **1982**, *21*, 4105.
(22) This sample was a gift from K. S. Hagen and R. H. Holm. See: Berg, J. M.; Holm, R. H. In *Iron-Sulfur Proteins*; Spiro, T. G., Ed.; Wiley: New York, 1982; Chapter 1.
(23) Marsh, R. E. *Acta Crystallogr.* **1952**, *5*, 458.

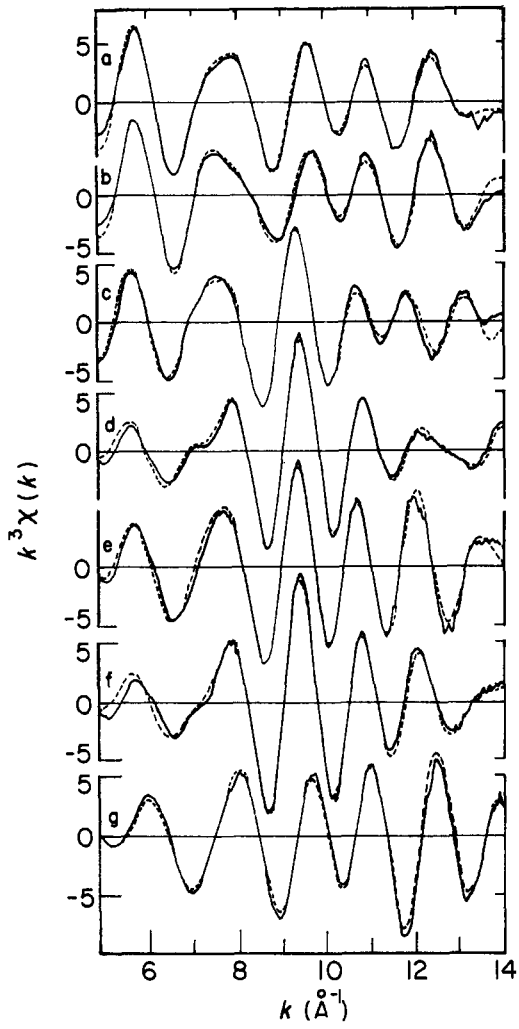

Figure 2. Curve-fitting results of four-shell fits for the Fe K-edge EXAFS data from (a) $(AsPh_4)_2[Fe_2S_2(NO)_4]$, (b) $Fe_2(\mu\text{-}SEt)_2(NO)_4$, (c) $Fe_2(\mu\text{-}SMe)_2(CO)_6$, (d) $Fe_2(Se_2)(CO)_6$, (e) $Li_2[Fe_2Se_2(CO)_6]$ (in THF solution), (f) $Fe_2(\mu\text{-}SePh)_2(CO)_6$, and (g) $Fe_2(\mu\text{-}SeBzl)_2(NO)_4$. Details of the simulation parameters are given in Table I. All data were collected on solid samples unless otherwise indicated. In each spectrum, the raw EXAFS data (—) are compared with the best simulation (---).

range $\mathbf{k}$ = 5–14 Å^{-1}. Once the amplitude and phase functions were selected for each shell (by using either empirically determined functions or theoretical functions with appropriate values for S_i, ΔE_0), the N_i value for that shell was selected and fixed (at some integer value) and initial estimates of R_i and σ_i^2 were selected. Only R_i and σ_i^2 were varied (for each shell) in the least-squares optimization. The validity of the selected N_i values was assessed by comparing σ_i^2 values with those of the structurally characterized dimers. Very little variation in σ_i^2 is expected for the same shells of such structurally related compounds.

Results and Discussion

Two classes of compounds were examined, carbonyl iron chalcogenides and nitrosyl iron chalcogenides. The iron carbonyls studied in this project may be subdivided according to the reaction sequence shown in eq 1.

The compounds $Fe_2(E_2)(CO)_6$ have been the subject of three crystallographic studies by Dahl and co-workers.[2,24] The structures feature closed tetrahedral Fe_2E_2 cores wherein each iron may be viewed as occupying a pseudooctahedral environment defined by three carbonyls, two chalcogen atoms, and the other iron center. In the present study, the structures of $Fe_2(E_2)(CO)_6$ were examined in the solid and in THF solution by Fe and Se EXAFS.

Figure 1 shows the results of data reduction and Fourier transformation of Fe EXAFS data for a solid sample of $Fe_2(S_2)(CO)_6$. The appearance of several beats in the EXAFS data (Figure 1c) indicates the presence of multiple shells of scattering atoms in the neighborhood of the Fe. These shells appear as a series of overlapping scattering peaks in the Fourier transform (Figure 1d). For $Fe_2(S_2)(CO)_6$, four separate shells of scattering atoms are expected: Fe–C, Fe–S, Fe–Fe, and Fe···O. Using the scattering functions described in the Experimental Section, curve-fitting analysis results in an excellent fit using four shells. The results of curve-fitting analysis for this and a number of related compounds are summarized in Figure 2 and Table I. Table I also compares our EXAFS results with the crystallographic results. Fourier transformation of the individual shells of the best fit simulation for $Fe_2(S_2)(CO)_6$ results in the assignment of Fourier transform peaks shown in Figure 3. As is typical throughout this series of compounds, the Fe–Fe Fourier transform peak is significantly obscured by other features and simple visual interpretation of Fourier transforms as a means of identifying the presence of an Fe–Fe interaction is clearly not feasible; we therefore relied on curve-fitting analyses for this identification.

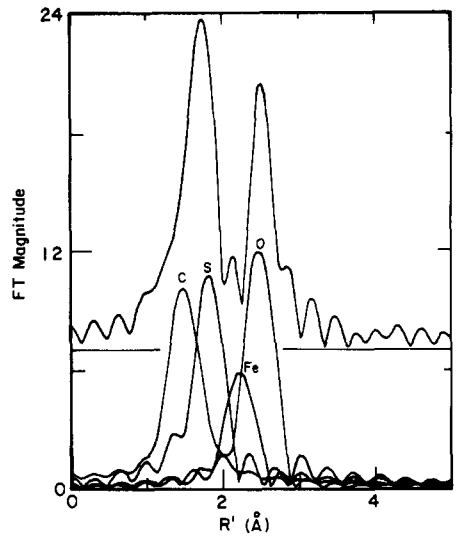

Figure 3. Deconvolution of the Fourier transform (FT) of Fe K-edge EXAFS data from a solid sample of $Fe_2(S_2)(CO)_6$. The top FT is the data of Figure 1d, and each shell of the best fit simulation (Figure 4a) was Fourier transformed ($\mathbf{k}$ = 5–14 Å^{-1}, $\mathbf{k}^3$ weighting) to give the four FTs in the bottom portion of the figure. Note that the Fe–Fe FT peak is significantly obscured by the other FT peaks and that the overall FT magnitude (upper portion) is *not* the simple sum of the FT magnitudes of the individual shells (bottom portion).

As shown in Table I, an Fe–Fe interaction is required to obtain a good simulation of the Fe EXAFS for all of the compounds examined in this study. The calculated Fe–Fe distances range from 2.52 to 2.57 Å for the CO-containing dimers and from 2.69 to 2.71 Å for the NO-containing dimers. These values compare favorably with crystallographically determined Fe–Fe bond lengths for $Fe_2(S_2)(CO)_6$ (2.55 Å),[2] $Fe_2(Se_2)(CO)_6$ (2.58 Å),[24] $Fe_2(\mu\text{-}SEt)_2(CO)_6$ (2.54 Å),[25] and $Fe_2(\mu\text{-}SEt)_2(NO)_4$ (2.72 Å).[18] The requirement of an Fe–Fe contribution was further tested by attempting curve fitting of the Fe EXAFS of $Fe_2(S_2)(CO)_6$ using only Fe–C, Fe–S, and Fe···O contributions: the results are shown in Figure 4. The absence of the Fe–Fe contribution results in a poor simulation, especially in the beat regions at $\mathbf{k} \simeq 7.5$ and 11.5 Å^{-1} (cf. Figure 4a,b).

We used Seyferth's Superhydride method to generate THF solutions of the highly reactive $[Fe_2E_2(CO)_6]^{2-}$ (eq 3).[8] On the

$$Fe_2(E_2)(CO)_6 + 2LiBHEt_3 \rightarrow Li_2[Fe_2E_2(CO)_6] + H_2 + 2BEt_3 \quad (3)$$

basis of their color and reactivity, the green dianions prepared in this way are the same as those prepared by more traditional, but less convenient, methods which involve the use of sodium

(24) Campana, C. F.; Lo, F. Y.-K.; Dahl, L. F. *Inorg. Chem.* **1979**, *18*, 3060.

(25) Dahl, L. F.; Wei, C.-H. *Inorg. Chem.* **1963**, *2*, 328.

Table I. Summary of Curve-Fitting Results for Fe K-Edge and Se K-Edge EXAFS Data[a]

	Fe–C, Fe–N		Fe···O		Fe–Fe		Fe–S, Fe–Se		Se–Fe		Se–Se		Se–C	
compound	R, Å	$\Delta\sigma^2$,[b] Å^2	R, Å	$\Delta\sigma^2$, Å^2	R, Å	$\Delta\sigma^2$, Å^2	R, Å	$\Delta\sigma^2$, Å^2	R, Å	$\Delta\sigma^2$, Å^2	R, Å	$\Delta\sigma^2$, Å^2	R, Å	$\Delta\sigma^2$, Å^2
$Fe_2(S_2)(CO)_6$ (solid)	1.78 (2)[c]	0.0025 (18)	2.96 (2)	0.0000 (13)	2.56 (3)	0.0000 (21)	2.21 (2)	0.0000 (13)						
	[1.78][d]		[2.92]		[2.55]		[2.23]							
$Fe_2(S_2)(CO)_6$ (in THF)	1.78 (2)	0.0022 (18)	2.96 (2)	−0.0004 (13)	2.57 (3)	−0.0005 (21)	2.22 (2)	0.0002 (13)						
$Li_2[Fe_2S_2(CO)_6]$ (in THF)	1.76 (2)	0.0020 (15)	2.96 (2)	−0.0004 (12)	2.54 (3)	0.0008 (21)	2.29 (2)	0.0003 (16)						
$Fe_2(\mu\text{-SMe})_2(CO)_6$ (solid)	1.78 (2)	0.0026 (16)	2.95 (2)	0.0005 (12)	2.52 (3)	−0.0008 (21)	2.24 (2)	0.0005 (14)						
	[1.81]		[2.96]		[2.54]		[2.26]							
$Fe_2(Se_2)(CO)_6$ (solid)	1.77 (3)	0.0028 (17)	2.94 (2)	0.0001 (12)	2.55 (3)	−0.0014 (14)	2.36 (2)	0.0000 (7)	2.35 (2)	0.0000 (9)	2.28 (2)	−0.0014 (7)		
	[1.79]		[2.95]		[2.58]		[2.36]		[2.36]		[2.29]			
$Fe_2(Se_2)(CO)_6$ (in THF)	1.77 (3)	0.0025 (17)	2.94 (2)	0.0000 (12)	2.54 (3)	−0.0012 (14)	2.35 (2)	−0.0002 (7)	2.33 (2)	−0.0037 (9)	2.32 (2)	−0.0018 (7)		
$Li_2[Fe_2Se_2(CO)_6]$ (in THF)	1.76 (3)	0.0017 (14)	2.95 (2)	−0.0003 (11)	2.57 (3)	−0.0023 (26)	2.40 (2)	−0.0002 (7)	2.40 (2)	−0.0004 (9)				
$Fe_2(\mu\text{-SePh})_2(CO)_6$ (solid)	1.77 (3)	0.0024 (16)	2.95 (3)	0.0000 (12)	2.54 (3)	−0.0029 (20)	2.37 (2)	−0.0003 (7)	2.38 (2)	−0.0010 (10)			1.92 (6)	0.0010 (45)
$Fe_2(\mu\text{-SeBzl})_2(CO)_6$ (in THF)	1.77 (3)	0.0026 (16)	2.94 (3)	0.0000 (12)	2.55 (3)	−0.0024 (20)	2.37 (2)	−0.0001 (7)	2.37 (2)	−0.0010 (9)			1.96 (6)	0.0005 (45)
$(AsPh_4)_2[Fe_2S_2(NO)_4]$ (solid)	1.66 (2)	0.0001 (15)	2.82 (8)	0.0088 (64)	2.70 (3)	−0.0022 (14)	2.23 (2)	−0.0008 (13)						
$Fe_2(\mu\text{-SEt})_2(NO)_4$ (solid)	1.67 (2)	0.0004 (15)	2.81 (8)	0.0106 (64)	2.69 (3)	−0.0023 (14)	2.25 (2)	−0.0004 (13)						
	[1.67]		[2.82]		[2.72]		[2.27]							
$Fe_2(\mu\text{-SeBzl})_2(NO)_4$ (solid)	1.66 (2)	0.0006 (15)	2.77 (4)	0.0035 (34)	2.71 (2)	−0.0029 (15)	2.36 (2)	−0.0001 (7)	2.36 (2)	−0.0009 (9)			1.99 (11)	0.0013 (63)

[a] The shells are indicated by the atom pairs A–B (or A···B) in which A denotes the absorbing atom and B denotes the backscattering atom (··· denotes that A and B are not directly bonded). Best fit (optimized) values for R (the A–B distance) and $\Delta\sigma^2$ (the relative mean-square deviation in R arising in general from both static disorder and vibrational contributions) are tabulated for each shell. All other parameters were not varied (see Experimental Section). Coordination numbers used for each shell: 3 (Fe–C); 2 (Fe–N); 3 or 2 (Fe···O in the CO or NO dimers, respectively); 1 (Fe–Fe); 2 (Fe–S and Fe–Se); 2 (Se–Fe); 1 (Se–Se); 1 (Se–C). [b] Relative mean-square deviation in R. For each shell, this is the difference between the σ^2 for the given compound and the σ^2 for a reference compound. Reference compounds used: Fe–C and Fe–N, $Fe_2(\mu\text{-SEt})_2(NO)_4$; Fe···O, $Fe(1,3\text{-}C_4H_6)(CO)_3$; Fe–Fe and Fe–S, $Fe_2(S_2)(CO)_6$; Fe–Se and Se–Fe, $Fe_2(Se_2)(CO)_6$; Se–Se and Se–C, PhSeSePh. [c] Numbers in parentheses are errors estimated by the following procedure: All parameters except for the one of interest were set to their optimized values and a goodness-of-fit statistic

$$f \equiv \{\sum_i [\mathbf{k}^3(\chi_{\text{obsd}}^{(i)} - \chi_{\text{calcd}}^{(i)})]^2/(N-1)\}^{1/2}$$

was calculated for a series of values of the parameter of interest. The estimated error was then taken as the largest absolute deviation of the parameter from its optimized value required to give an f statistic that was twice the optimized f. [d] The distances given in brackets are crystallographically determined. For the following compounds, these data were taken from the indicated reference: $Fe_2(S_2)(CO)_6$, ref 2; $Fe_2(\mu\text{-SEt})_2(CO)_6$, ref 25; $Fe_2(Se_2)(CO)_6$, ref 24; $Fe_2(\mu\text{-SEt})_2(NO)_4$, ref 18.

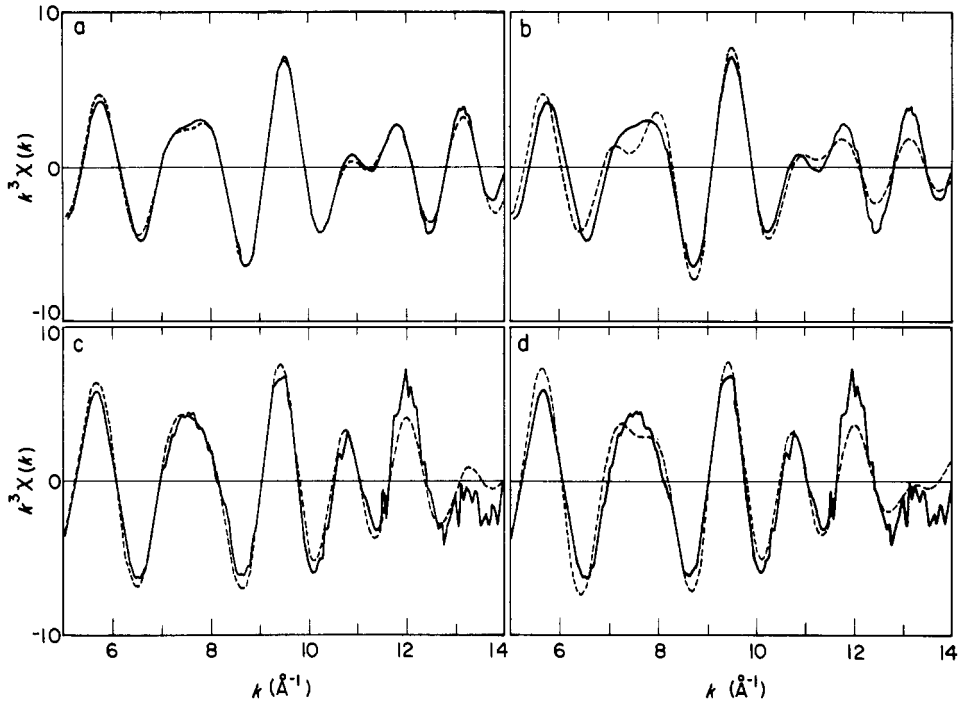

Figure 4. Comparison of simulations of Fe K-edge EXAFS data using four shells (Fe–C, Fe–S, Fe–Fe, Fe···O) (a, c) with simulations using three shells (Fe–C, Fe–S, Fe···O) (b, d). (a) and (b) are results on a solid sample of $Fe_2(S_2)(CO)_6$ and (c) and (d) are results on a THF solution of $Li_2[Fe_2S_2(CO)_6]$. This comparison demonstrates that the Fe–Fe interaction must be included in order to properly simulate the EXAFS data.

amalgam.[26] Because of the extreme air sensitivity of these species, we employed a special solution cell (see Experimental Section).

The Fe EXAFS of the THF solutions of $Li_2[Fe_2E_2(CO)_6]$ were only subtly different from the corresponding data for their natural precursors. In particular the changes in Fe–Fe and Fe–C distances were less than 0.03 Å. The requirement for an Fe–Fe contribution was further tested by attempting curve fitting of the Fe EXAFS of the $[Fe_2S_2(CO)_6]^{2-}$ with only Fe–C, Fe–S, and Fe···O contributions (Figure 4). Neglect of the Fe–Fe interaction resulted in a poor simulation especially at $\mathbf{k}$ = 7.5 Å^{-1}. This analysis supports the conclusion that the Fe–Fe bond is substantially unchanged upon the two-electron reduction of $Fe_2(E_2)(CO)_6$ (E = S, Se).

To further explore the structure of the dianions, the local environment of Se in $[Fe_2Se_2(CO)_6]^{2-}$ was compared to that in $Fe_2(Se_2)(CO)_6$ by using Se EXAFS. As described in the Experimental Section, PhSeSePh was examined by Se EXAFS to derive the scattering function for a Se–Se interaction. The Fourier transforms of the Se EXAFS of PhSeSePh, $Fe_2(Se_2)(CO)_6$, and $[Fe_2Se_2(CO)_6]^{2-}$ are compared in Figure 5. The approximately twofold increase in the scattering amplitude in $Fe_2(Se_2)(CO)_6$ (Figure 5b) compared to that in PhSeSePh (Figure 5a) is due to the Se–Fe contribution, and a scattering function for that contribution was extracted from the $Fe_2(Se_2)(CO)_6$ data. The Se EXAFS Fourier transform of $[Fe_2Se_2(CO)_6]^{2-}$ (Figure 5c) shows a single peak again about half the size of the peak for $Fe_2(Se_2)(CO)_6$. The Se–Fe interaction must still be present in $[Fe_2Se_2(CO)_6]^{2-}$ and the Fourier transform peak is well simulated, assuming no other neighbors (see Table I). Furthermore, the Fe–Se distances obtained from Se EXAFS and Fe EXAFS are in close agreement. Two explanations are possible for the absence of a significant Se–Se contribution to the FT in Figure 5c. The separation between Se atoms could be too large (up to a maximum of 4.05 Å determined by the core geometry of the dianion, given the Fe–Se and Fe–Fe bond lengths of Table I) to observe any significant Se–Se scattering. Alternatively, the Se bridges could display large uncorrelated vibrational motion, resulting in a large σ_i^2 for the Se–Se interaction. For example, hypothesizing an average Se–Se separation of 3.3 Å (corresponding to a dihedral

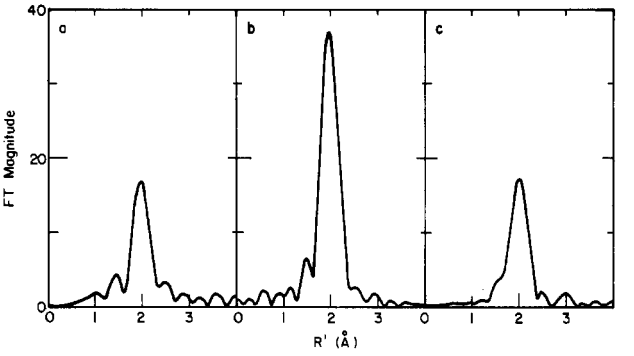

Figure 5. Fourier transforms ($\mathbf{k}$ = 3.5–14.5 Å^{-1}, $\mathbf{k}^3$ weighting) of Se K-edge EXAFS data for (a) PhSeSePh, (b) $Fe_2(Se_2)(CO)_6$, and (c) $Li_2[Fe_2Se_2(CO)_6]$ (in THF). The major FT peak results from (a) Se–Se scattering, (b) both Se–Se and Se–Fe scattering, and (c) only Se–Fe scattering. The significantly reduced intensity of the $[Fe_2Se_2(CO)_6]^{2-}$ FT peak (c) compared to that of $Fe_2(Se_2)(CO)_6$ (b) demonstrates the absence of a detectable Se–Se interaction in the former compound.

angle of 110° between the two Fe_2Se planes), we estimate that $\Delta\sigma^2$ would need to be >0.013 Å^2 for the Se–Se peak not to be observable above the noise in Figure 5c. With an unchanged Se–Se distance of 2.2 Å, a very similar value of $\Delta\sigma^2$ would be necessary for the FT peak of Figure 5c not to have a significant (>10%) contribution from Se–Se scattering. Assuming a simple harmonic oscillator model and a typical Se–Se single-bond stretching frequency of ~250 cm^{-1}, as found in $(PPh_4)_2Fe_2(Se)_2(Se_5)_2$,[27] this $\Delta\sigma^2$ corresponds to a stretching frequency of about 100 cm^{-1} in the dianion, which is completely inconsistent with the presence of a normal Se–Se bond. We therefore find no evidence for the existence of a Se–Se bond in $[Fe_2Se_2(CO)_6]^{2-}$. *It is apparent that the two-electron reduction of $Fe_2(E_2)(CO)_6$ (E = S, Se) results in cleavage of the E–E bond.*

Our studies on the structural consequences of the reduction of $Fe_2(E_2)(CO)_6$ were supplemented by characterization of the alkylated derivatives (eq 4). The core structures of these orga-

$$[Fe_2E_2(CO)_6]^{2-} + 2RX \rightarrow Fe_2(\mu\text{-}ER)_2(CO)_6 + 2X^- \quad (4)$$

(26) Seyferth, D.; Henderson, R. S. *J. Am. Chem. Soc.* **1979**, *101*, 508.

(27) Strasdeit, H.; Krebs, B.; Henkel, G. *Inorg. Chim. Acta* **1984**, *89*, L11.

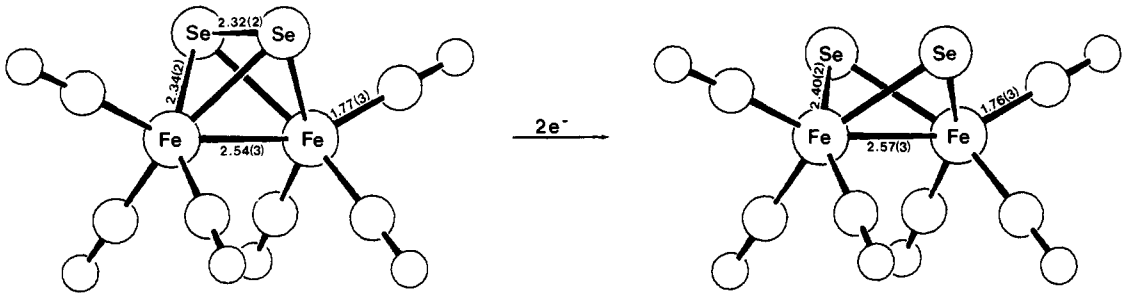

Figure 6. Solution structures of $Fe_2(Se_2)(CO)_6$ and $[Fe_2Se_2(CO)_6]^{2-}$ obtained from Fe and Se EXAFS data (Table I).

nochalcogen compounds are presumed to be structurally similar to that of $[Fe_2E_2(CO)_6]^{2-}$. It should be noted that these compounds can exist in three isomeric forms that differ in the relative orientations of the organic substituent on the chalcogen.[28] This isomerism is expected to induce only slight perturbations on the structure of the Fe_2E_2 core. The Fe EXAFS confirms that the coordination environment about iron is similar in the dianions and their alkylated derivatives. Our results on $Fe_2(\mu\text{-}SMe)_2(CO)_6$ are in accord with the results of Dahl's crystallographic studies on the μ-SEt compound.[24] Furthermore, there is good agreement between the Fe–Se distances derived from the Fe and Se EXAFS on $Fe_2(\mu\text{-}SePh)_2(CO)_6$. This Fe–Se distance of 2.38 Å is intermediate with respect to the corresponding distances in $Fe_2(Se_2)(CO)_6$ and $[Fe_2Se_2(CO)_6]^{2-}$.

Roussin's red anion $[Fe_2S_2(NO)_4]^{2-}$ was the first soluble metal sulfide characterized and is obviously related to $[Fe_2S_2(CO)_6]^{2-}$. Recent years have witnessed a resurgence of interest in this nitrosyl compound with regard to its reactivity,[13,15,29] its relationship to the Fe–S–CO system,[30] and the biological activity of its derivatives.[31] The structure of Roussin's red anion has only been recently studied crystallographically in the form of its potassium salt.[32] The structure, although of low precision, confirms the gross features as resembling that for $Fe_2(\mu\text{-}SEt)_2(NO)_4$. Our Fe and Se EXAFS studies confirm these findings.

The Fe EXAFS of $(AsPh_4)_2[Fe_2S_2(NO)_4]$, $Fe_2(\mu\text{-}SEt)_2(NO)_4$, and $Fe_2(\mu\text{-}SeBzl)_2(NO)_4$ were studied.[13] The Fe–Fe distances in this series of compounds fall in the narrow range of 2.69–2.71 Å and as such are ca. 0.15 Å longer than those found in the carbonyl compounds. On the other hand, the Fe–E distances closely resemble those in the carbonyls. It can also be seen that ethylation of $[Fe_2S_2(NO)_4]^{2-}$ results in very modest structural changes. These results indicate that μ-S^- is electronically equivalent to μ-SR in this series of nitrosyl dimers. This finding is in accord with our results on $[Fe_2S_2(CO)_6]^{2-}$ and $Fe_2(\mu\text{-}SR)_2(CO)_6$.

Conclusions

In this paper we have delineated the essential structural changes that occur upon the two-electron reduction of the compounds $Fe_2(E_2)(CO)_6$ (E = S, Se). The Fe EXAFS results clearly show that the addition of two electrons to these tetrahedranes results in only small changes in the Fe–Fe distances. On the other hand, the Se EXAFS shows that the Se–Se bond in $Fe_2(Se_2)(CO)_6$ is absent in the dianion. It should be noted that in other respects the EXAFS-derived Fe···X (X = C, O, S, Se) distances are fairly normal and compare favorably with literature precedents.

On the basis of the present results, the structure of $[Fe_2E_2(CO)_6]^{2-}$ (E = S, Se) is that shown in Figure 6. This result, together with Averill's characterization of $(AsPh_4)_2[Fe_2S_2(CO)_6]_2$,[33,34] allows us to depict the complete reduction sequence for $Fe_2(S_2)(CO)_6$ (eq 5). A related but more novel reduction

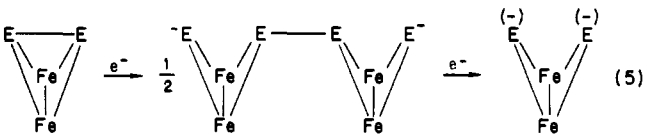

(5)

sequence starting with the cubane $Fe_4S_4(CO)_{12}$ can be envisioned.[35] Systematic study of the latter sequence is, however, hampered by the virtual insolubility of $Fe_4S_4(CO)_{12}$.[9]

The present results are also relevant to the mechanism of charge storage by metal trichalcogenides such as $NbSe_3$[36] and MoS_3.[37] These low-dimensional compounds are comprised of linear chains of tetrahedral M_2E_2 subunits. Previous work has suggested that reduction of $NbSe_3$ (i.e., $Nb(Se_2)Se$) induces lysis of the Se–Se bonds.[36] Additionally, chemical or electrochemical reduction of amorphous MoS_3 (i.e., $Mo(S_2)S$) also appears to involve breaking of the S–S bonds.[37] Our results show that $Fe_2E_2(CO)_6^{0/2-}$ is a molecular model for these solid-state transformations.

Acknowledgment. This research was supported by the National Science Foundation (Grants NSF CHE-84-10779 to T.B.R. and DMB 85-02707 to R.A.S.). X-ray absorption measurements were performed at the Stanford Synchrotron Radiation Laboratory, which is supported by the Department of Energy, Office of Basic Energy Sciences, and the National Institutes of Health, Biotechnology Resource Program, Division of Research Resources.

Registry No. $Fe_2(S_2)(CO)_6$, 14243-23-3; $Li_2[Fe_2S_2(CO)_6]$, 74438-48-5; $Fe_2(\mu\text{-}SMe)_2(CO)_6$, 14878-96-7; $Fe(Se_2)(CO)_6$, 76185-26-7; $Li_2[Fe_2Se_2(CO)_6]$, 76683-33-5; $Fe_2(\mu\text{-}SePh)_2(CO)_6$, 25987-99-9; $Fe_2(\mu\text{-}SeBzl)_2(CO)_6$, 101348-76-9; $(AsPh_4)_2[Fe_2S_6(NO)_4]$, 79408-07-4; $Fe_2(\mu\text{-}SEt)_2(NO)_4$, 15020-36-7; $Fe_2(\mu\text{-}SeBzl)_2(NO)_4$, 79919-44-1; $Fe_2(\mu\text{-}I)_2(NO)_4$, 15002-08-1; $(AsPh_4)_2[Fe_2Se_2(NO)_4]$, 101348-78-1; Fe, 7439-89-6; Se, 7782-49-2.

(28) King, R. B. *J. Am. Chem. Soc.* **1962**, *84*, 2460.
(29) Butler, A. R.; Glidewell, C.; McGinnis, J. *Inorg. Chim. Acta* **1982**, *64*, L77. Glidewell, C.; McGinnis, J. *Inorg. Chim. Acta* **1982**, *64*, L171.
(30) Seyferth, D.; Gallagher, M. K. *J. Organomet. Chem.* **1981**, *218*, C5.
(31) Lu, S.-H.; Camus, A.-M.; Tomatis, L.; Barstch, H. *J. Natl. Cancer Inst. (U.S.)* **1981**, *66*, 33. Ashworth, J. J.; Didcock, A.; Hargreaves, L. L.; Jarvis, B.; Walters, C. L.; Larkworthy, L. F. *J. Gen. Microbiol.* **1974**, *84*, 403.
(32) Lin, X.; Huang, J.; Lu, J. *Acta Crystallogr., Sect. A: Cryst. Phys., Diffr., Theor. Gen. Crystallogr.* **1984**, *3*, 1127.
(33) Bose, K. S.; Sinn, E.; Averill, B. A. *Organometallics* **1984**, *3*, 1127.
(34) Seyferth, D.; Kiwan, A. M.; Sinn, E. *J. Organomet. Chem.* **1985**, *281*, 111.
(35) Nelson, L. L.; Lo, F. Y.; Rae, A. D.; Dahl, L. F. *J. Organomet. Chem.* **1982**, *225*, 309.
(36) Rouxel, J. *Rev. Inorg. Chem.* **1979**, *1*, 245.
(37) Scott, R. A.; Jacobson, A. J.; Chianelli, R. R.; Pan, W.-H.; Stiefel, E. I.; Hodgson, K. O.; Cramer, S. P. *Inorg. Chem.*, preceding paper in this issue.